

pubs.acs.org/cm Article

Understanding the Role of Charge Storage Mechanisms in the Electrochromic Switching Kinetics of Metal Oxide Nanocrystals

Hsin-Che Lu, Benjamin Z. Zydlewski, Bharat Tandon, Sofia A. Shubert-Zuleta, and Delia J. Milliron*



Cite This: Chem. Mater. 2022, 34, 5621-5633



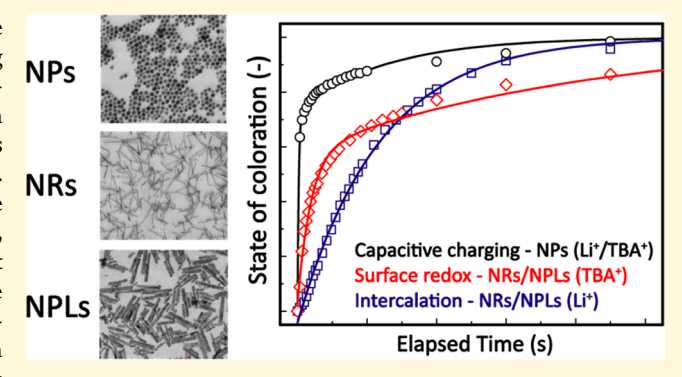
ACCESS

Metrics & More

Article Recommendations

s Supporting Information

ABSTRACT: The development of electrochromic metal oxide nanocrystals holds promise for improving the sluggish switching kinetics of conventional electrochromic smart windows. Nevertheless, the microscopic processes controlling switching kinetics in nanocrystals may differ from those in traditional bulk materials where ion diffusion following intercalation is often rate limiting. Herein, by systematically investigating the electrochromic response of Sn-doped $\rm In_2O_3$ nanoparticles, orthorhombic $\rm Nb_2O_5$ nanorods, and monoclinic $\rm Nb_{12}O_{29}$ nanoplatelets, we elucidate how different charge storage mechanisms, including capacitive charging, surface redox, and intercalation, affect the switching kinetics of electrochromic nanocrystals. The nanocrystals were reduced in both lithium- and tetrabutylammonium-based electrolytes at various



potentials to determine which charge storage mechanism governs their electrochromic response, and the optical switching kinetics at a reducing potential were quantified by fitting with an exponential-growth model based on the charging behavior of capacitors. For the surface-dominated capacitive charging and surface redox mechanisms, dual-stage switching kinetics were observed regardless of the materials, switching rapidly at the early stage of reduction and becoming slower over time as charge accumulates in the electric double layer. As for the intercalation mechanism, single-stage switching kinetics controlled by the reaction rate of ion intercalation were observed. By using spectroelectrochemical methods, we demonstrated approaches to define the charge storage mechanisms in electrochromic metal oxide nanocrystals and investigated how these mechanisms affect the switching kinetics of the electrochromic response.

■ INTRODUCTION

To mitigate the increasing building energy consumption for maintaining a comfortable indoor environment, electrochromic smart windows are designed to reduce the energy use associated with lighting, heating, and cooling. 1,2 By applying an external potential bias to the electrochromic smart windows, the active electrochromic layers change their transmittance according to the electrochemical reactions, and thus, the solar spectrum transmitting through the windows can be modulated. 1,2 To date, thin films of bulk transition-metal oxides are the dominant materials for commercialized electrochromic smart windows due to their broad electrochromic spectral change across the visible and near-infrared regions and ideal electrochemical and optical stabilities.³ However, the switching kinetics of bulk transition-metal oxides are significantly limited by the ion diffusion rate during the intercalation of ions following redox reaction. 4-6 The sluggish ion diffusion often leads to undesired long switching time up to minutes in labscale electrochromic devices or more than 10 min in large-scale electrochromic smart windows. To address this, methods focusing on altering the electrochemical mechanisms have been proposed to improve the switching kinetics. Nanocrystals of transition-metal oxides were synthesized and applied as

electrochromic layers to mitigate the influence of Li⁺ intercalation by minimizing diffusion path length.^{7–12} In this regard, electrochromic coloration mechanisms can differ from the Li⁺ intercalation typically operating in bulk transition-metal oxides, with other mechanisms such as capacitive charging and surface redox becoming dominant in some cases.^{4,13,14} Alternatively, plasmonic metal oxide nanocrystals were synthesized with the ability to modulate their transmittance spectrum by capacitive charging only, which circumvents the slow ion diffusion rate in bulk transition-metal oxides.¹⁵ Both approaches rely on the precision of colloidal nanocrystal synthesis that offers better control over crystal structure, crystallite morphology, and electrochromic properties compared to conventional film deposition methods.^{9,16} As a consequence of altering the electrochemical mechanisms, in

Received: March 27, 2022 Revised: May 25, 2022 Published: June 8, 2022





terms of switching kinetics, the microscopic processes limiting the overall rate can be drastically different for nanoscale materials. ¹⁷ It is necessary to consider the contributions from both the typical Li⁺ intercalation and other surface-dominated mechanisms that are more prominent on the nanoscale. Yet, the complex relationship between the electrochromic switching kinetics and various electrochemical mechanisms has not been well understood. Thus, we sought to systematically investigate the electrochemical mechanisms that determine the electrochromic switching kinetics of metal oxide nanocrystals to better design them for and utilize them in electrochromic smart windows.

The electrochromic response of metal oxides emerges upon charge being injected into or extracted from the material during electrochemical reaction. In cathodic coloring electrochromic metal oxides, in which transmittance decreases upon electron injection, the charge can be stored through various electrochemical mechanisms and concurrently ions will be stored for charge balance. The traditional optical mechanism in transition-metal oxides comes from the electrochemical reduction of metal ions together with ion intercalation (mostly Li⁺), ¹⁸ commonly activating polaronic absorption, as reported in tungsten(VI) oxides, niobium(V) oxides, and titanium(IV) oxides. 19-21 In other cases, the optical response of transitionmetal oxides is triggered by redox reaction, but with little evidence of ion intercalation.²² This phenomenon has been described as surface redox with ions only adsorbed on the surface of the oxides to compensate for the additional charge, as reported in some anodic coloring electrochromic metal oxides such as nickel (II) oxides, manganese(IV) oxides, etc.^{23,24} Finally, in some metal oxide nanocrystals, such as nanocrystals of doped indium(III) oxide, the optical response can be activated by localized surface plasmon resonance (LSPR), where the decreasing transmittance is the result of collective resonance of charge carriers being injected into the nanocrystals. 15,25 The electrochemical process does not depend on redox reaction and the additional charge carriers can be balanced by capacitive charge, where desolvated cations are adsorbed in the electric double layer (EDL) near the surface of the nanocrystals and solvated cations are located in the outer diffuse layer of the EDL.¹⁵

The diverse nature of charging mechanisms makes it difficult to propose a generalized model for switching kinetics applicable to all electrochromic metal oxide nanocrystals. The role of diffusion in governing the switching kinetics of nanocrystals is unclear since the characteristic diffusion path length l ($l = (2Dt)^{1/2}$, where D is the diffusion coefficient and tis the characteristic time) is close to the particle size. ¹⁷ Owing to this correspondence, ion diffusion can be less influential in nanocrystals compared to their bulk counterparts. In addition, the high surface area of nanocrystals amplifies the importance of surface redox or capacitive charging, which become more significant charge storage mechanisms. It is also worth noting that the electrochromic response of metal oxide nanocrystals is compatible with a broad range of cations, including Li⁺, Na⁺, K⁺, Al⁺, and tetrabutylammonium (TBA⁺), for the purpose of tuning the electrochromic properties associated with different charge storage mechanisms. ^{10,15,16,26–28} The choice of cations not only affects the diffusion rate during ion intercalation and in the bulk electrolyte ^{29,30} but also determines whether intercalation is allowed based on the relative size of the cation compared to the size of the interstitial sites in the crystal lattice. 10,13 Previous studies have modeled the electrochromic

transmittance change over time of conducting polymer films using an exponential-growth equation derived from the charging behavior of capacitors. The week, the charge storage mechanisms of metal oxides, and the associated microscopic processes governing kinetics, are distinct from organic polymers. To better facilitate the design of metal oxide nanocrystals for fast switching kinetics, we aimed at understanding the interplay between charge storage mechanisms and switching kinetics of metal oxide nanocrystals when reduced in the presence of various cations.

For this investigation, we synthesized and fabricated films of three distinct types of metal oxide nanocrystals, including Sndoped In₂O₃ nanoparticles (NPs), orthorhombic Nb₂O₅ nanorods (NRs), and monoclinic Nb₁₂O₂₉ nanoplatelets (NPLs), for the purpose of systematically exploring the switching kinetics associated with different charge storage mechanisms. 8,10,15 Each of these nanocrystals shows different electrochromic signatures brought by various charge storage mechanisms, namely, capacitive charging (in NPs), surface redox (in NRs and NPLs), or ion intercalation (in NRs and NPLs), enabling us to explore the switching kinetics of these mechanisms individually. The electrochromic properties of the nanocrystals were examined in both Li+-based electrolytes and TBA+-based electrolytes. Because of the bulky nature of TBA+, intercalation into the crystal lattice is not allowed and the desolvated TBA+ can only be adsorbed on the surface of nanocrystals, while for Li+, intercalation dominates the electrochromism. With this understanding, the dependence of the electrochromic response of nanocrystals on the electrochemical redox of metal ions can be used as a feature to distinguish between capacitive charging and surface redox. Meanwhile, by using cations with different sizes, electrochromic response activated by ion intercalation only can be observed in Li⁺ but not in TBA⁺, allowing us to determine, during redox reactions, if the kinetics are governed by ion intercalation or surface redox. Furthermore, we propose a kinetic model to fit and analyze the electrochromic response over time under various charge storage mechanisms in the presence of Li+ and TBA+. By using multiple exponentialgrowth equations to fit the dynamic electrochromic response, we quantitively investigate the electrochromic switching kinetics of nanocrystals activated by different charge storage mechanisms. Overall, our goal is to demonstrate how the charge storage mechanism affects the electrochromic switching kinetics of various metal oxide nanocrystals and also explore the underlying processes that can improve the design of electrochromic smart windows to show rapid switching.

■ EXPERIMENTAL SECTION

Materials. Tin(IV) acetate (99.99%), toluene (>99.5%), acetone (>99.5%), isopropanol (>99.5%), hexane (>99%), N-dimethylformamide (DMF, anhydrous 99.8%), nitrosonium tetrafluoroborate (NOBF₄, 95%), niobium chloride (NbCl₅, anhydrous, 99.995%), oleic acid (90%), oleyl alcohol (85%), octadecene (90%), lithium perchlorate (LiClO₄, 99.99%), tetrabutylammonium perchlorate (TBAClO₄, 99%), and propylene carbonate (PC, anhydrous, 99.7%) were purchased from Sigma-Aldrich. Indium(III) acetate (≥99.99%) was purchased from STREM. Ethanol (90%) was purchased from Fischer Chemical. Oleylamine (90%) was purchased from Acros Organics. Before use, oleic acid, oleylamine, and octadecene were degassed at 120 °C under vacuum using a Schlenk line and stored in a N₂ glovebox.

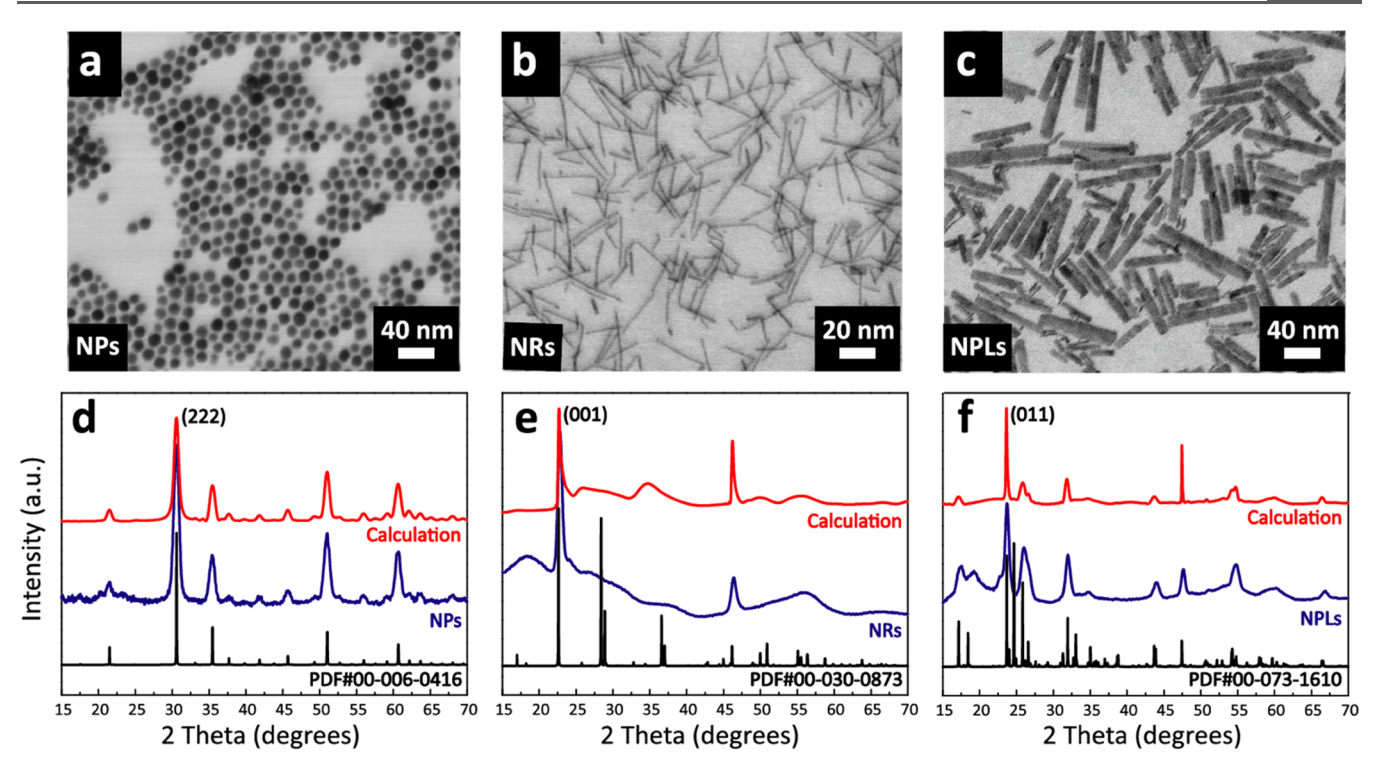


Figure 1. (a, b, c) Morphological characterization using bright-field STEM images of NPs, NRs, and NPLs. (d, e, f) Structural characterization of NPs, NRs, and NPLs by experimental XRD patterns (blue), calculated patterns (red), and reference patterns (black).

Nanocrystal Synthesis. The syntheses of NPs, NRs, and NPLs were carried out under a $\rm N_2$ atmosphere using Schlenk line techniques.

In the synthesis of NPs, or Sn-doped In2O3 nanocrystals, a slowinjection synthetic procedure was used. 33,34 In brief, the metal ion precursors were mixed in a molar ratio of 1:9 (Sn/In) and dissolved in oleic acid to obtain a 0.5 M solution in a flask. The precursor solution was first degassed at 100 °C under vacuum for 1 h and subsequently heated and kept at 150 °C for 2 h under a N2 atmosphere. In the meantime, 13 mL of oleyl alcohol was heated and kept at 290 °C in another flask under a N₂ atmosphere. By using a syringe pump, 1.5 mL of the as-prepared precursor solution was injected into the hot oleyl alcohol at a rate of 0.35 mL/min. After the injection, the mixed solution consisting of nanocrystals was washed using hexane as the solvent for dispersion and ethanol as the antisolvent for flocculation. The purified nanocrystals were dispersed in hexane at a concentration of 50 mg/mL, referred to as ligand-capped NPs. As characterized in our previous publication, the Sn% in NPs is 13.2% among all of the metal ions.3

The synthesis of NRs, or orthorhombic $\mathrm{Nb}_2\mathrm{O}_5$ nanocrystals, was adapted from our previous publication. In short, 2 mmol NbCl_5 was dissolved in a mixed solution in a flask containing 11 mmol oleic acid, 40 mmol octadecene, and 2 mmol oleylamine inside a N_2 glovebox. The flask was then transferred to a Schlenk line, degassed under vacuum at 100 °C for 1 h, heated to 240 °C, and reacted for 30 min under a N_2 atmosphere. After the reaction, the mixed solution was washed using hexane as the solvent and isopropanol as the antisolvent. Thereafter, the purified nanocrystals were redispersed in hexane at a concentration of 30 mg/mL, referred to as ligand-capped NRs.

The procedure for the synthesis of NPLs, or monoclinic $\mathrm{Nb}_{12}\mathrm{O}_{29}$ nanocrystals, can be found in our previous publication. ¹⁰ First, 1.5 mmol NbCl₅ was dissolved in 15 mmol oleic acid in a flask inside a N_2 glovebox. The flask was then transferred to a Schlenk line, heated at 40 °C under vacuum for 30 min, and heated to 120 °C under vacuum. In another flask, 40 mmol oleic acid and 8 mmol oleylamine were degassed at 120 °C for 30 min under vacuum and then heated to 300 °C under a N_2 atmosphere. The precursor solution in the first flask was switched to a N_2 atmosphere and was quickly injected into the

hot solution at 300 °C in the second flask and reacted for 10 min. Afterward, the mixed solution was washed using hexane as the solvent and isopropanol as the antisolvent. The resulting nanocrystals were dispersed in hexane at 15 mg/mL, referred to as ligand-capped NPLs.

Ligand-Stripping Procedure. The ligand-capped nanocrystal dispersions were diluted to 10~mg/mL, and a solution of NOBF_4 in DMF (10~mg/mL) was prepared for removing the ligands from the nanocrystal surfaces. In a typical procedure, an equal volume of NOBF_4 in DMF was gradually added to the nanocrystal dispersion and stirred for 30 min. The lower-layer solution containing a ligand-stripped nanocrystal was extracted and washed using DMF as the solvent and toluene as the antisolvent. After purification, the ligand-stripped nanocrystals were dispersed in DMF at 50~mg/mL and stored for film deposition.

Nanocrystal Film Deposition. Sn-doped $\rm In_2O_3\text{-}coated}$ glasses (20 $\Omega/\rm sq$, from Thin Film Devices) and Si wafers were used as substrates for spectroelectrochemical experiments and imaging purposes, respectively. Before use, the substrates were cleaned by sequentially sonicating in 2 vol % Hellmanex/deionized water, acetone, and isopropanol for 30 min each and subsequently treated with a UV ozone generator for 30 min. Twenty microliters of the ligand-stripped nanocrystal dispersion in DMF was spin-coated onto the substrates, at 1500 rpm for NPs and NRs and at 250 rpm for NPLs. The film-coated substrates were dried at 150 °C for 10 min before use.

Electron Microscopy Imaging. A Hitachi S5500 microscope was used for imaging. The films on Si substrates were imaged in scanning electron microscopy (SEM) mode, and the ligand-capped nanocrystal dispersion was dropped onto carbon-coated copper grids (400 mesh, Ted Pella) and dried under vacuum before imaging in scanning transmission electron microscopy (STEM) mode.

X-ray Diffraction (XRD) Analysis. Precipitated powders of the nanocrystals were collected by adding excess amounts of ethanol to ligand-capped nanocrystal dispersion. Afterward, the resulting cloudy solution was dried and the precipitated powder was mounted onto cryoloops (Hampton Research) with mineral oil. A Rigaku R-Axis Spider (1.54 Å Cu K α radiation) was used for measurement. To support the XRD analysis of the patterns obtained experimentally,

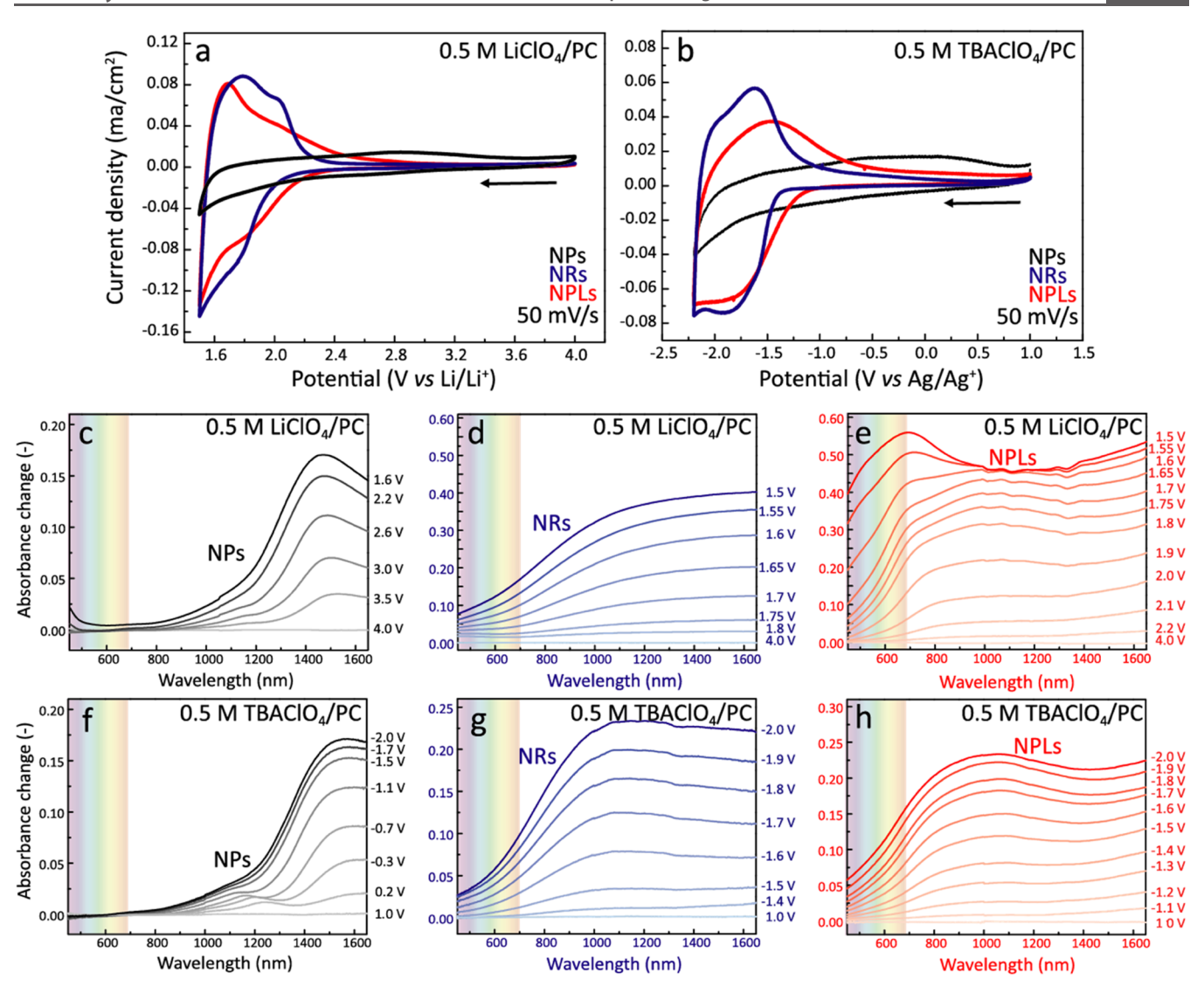


Figure 2. (a, b) Cyclic voltammograms of the films of NPs (black), NRs (blue), and NPLs (red) measured in 0.5 M LiClO₄/PC (ν s Li/Li⁺) and 0.5 M TBAClO₄/PC (ν s Ag/Ag⁺) at 50 mV/s. (c-h) Absorbance change of the films of NPs (black), NRs (blue), and NPLs (red) in 0.5 M LiClO₄/PC (ν s Li/Li⁺) and 0.5 M TBAClO₄/PC (ν s Ag/Ag⁺) when reduced at different potentials from 4.0 V (ν s Li/Li⁺) and 1.0 V (ν s Ag/Ag⁺) for 5 min using chronoamperometry.

simulations were performed based on the Debye scattering formula. Details of this calculation method can be found in previous publications. ^{9,10,35,36} A crystal visualization program, VESTA, ³⁷ was used to generate the atomistic models for the calculations.

Spectroelectrochemical Measurement. Electrochemical experiments were performed in an Ar glovebox using a Bio-logic VMP3 potentiostat. Concurrently, an ASD Quality Spec Pro spectrometer was used to collect the optical transmittance change of nanocrystal films during electrochemical reaction. Homemade electrochemical cells were used for measurements, in which the nanocrystal films served as the working electrode, Li foils served as both counter and reference electrodes, and solutions of 0.5 and 0.02 M LiClO₄ dissolved in PC (0.5 M LiClO₄/PC and 0.02 M LiClO₄/ PC) as the electrolyte. In experiments using the TBA-based electrolyte, the nanocrystal films served as the working electrode, Pt foils as the counter electrode, with a commercial fritted Ag/Ag+ reference electrode, and solutions of 0.5 and 0.02 M TBAClO₄ dissolved in PC (0.5 M TBAClO $_4$ /PC and 0.02 M TBAClO $_4$ /PC) as the electrolyte. Electrochemical techniques were applied by the potentiostat to the cell, including cyclic voltammetry, chronoamperometry, and electrochemical impedance spectroscopy (EIS).

■ RESULTS AND DISCUSSION

Morphological and Structural Characterizations. The STEM images of ligand-capped nanocrystals, including Sndoped In₂O₃, orthorhombic Nb₂O₅, and monoclinic Nb₁₂O₂₉, are shown in Figure 1a-c, respectively. Based on their morphology, the spherical particles of Sn-doped In₂O₃ are referred to as nanoparticles (NPs), the one-dimensional orthorhombic Nb₂O₅ as nanorods (NRs), and the twodimensional monoclinic Nb₁₂O₂₉ as nanoplatelets (NPLs). The average dimension of NPs was found to be 12.2 \pm 1.9 nm in diameter, the dimension of NRs was 39.2 ± 8.7 nm on the long axis and roughly 1 nm on the short axis, and the dimension of NPLs is 91.3 ± 28.5 nm on the long axis and 9.5 \pm 2.4 nm on the short axis. The crystal structures of the nanocrystals were characterized by comparing their experimental XRD patterns to both calculated patterns and reference patterns, as shown in Figure 1d-f. The atomistic models used for XRD simulations were constructed by using the unit cell of bixbyite In₂O₃, orthorhombic Nb₂O₅, and monoclinic Nb₁₂O₂₉, as presented in Figure S1. The XRD

pattern of NPs (Figure 1d) aligns well with the calculated pattern and the reference pattern of bixbyite In₂O₃ (PDF#00-006-0416), also in good agreement with the previous publication.³⁸ Both the NRs and NPLs are anisotropic crystals that extend only along a certain crystallographic direction of the unit cell.^{8,10} The validation of their crystal structures and morphologies was through simulations based on the Debye scattering formula for generating calculated XRD patterns. By comparing the experimental patterns to both calculations and references, the pattern of the NRs (Figure 1e) aligns well with calculation based on orthorhombic Nb₂O₅ (PDF#00-030-0873) extending only in the c direction, and the pattern of NPLs (Figure 1f) aligns with calculation based on monoclinic $Nb_{12}O_{29}$ (PDF#01-073-1610) extending only in the b and c directions, being one unit cell thick in the a direction. The calculated patterns for simulating the structure of NRs and NPLs indicate that the anisotropic nature of NRs and NPLs causes broadening or even disappearance of some reflections in the reference pattern due to the lack of constructive interference in certain crystallographic directions. 10 Figure S1 shows the atomistic models used in the XRD calculations that were designed with similar dimension to the nanocrystals shown in the STEM images.

Spectroelectrochemical Properties. Before spectroelectrochemical analysis, the ligand-capped nanocrystals were treated with a previously reported ligand-stripping procedure to increase the conductivity of nanocrystal films. Thereafter, the ligand-stripped nanocrystals were deposited onto ITO-coated glass substrates as films for spectroelectrochemical characterization, while the films on Si substrates were used for SEM imaging purposes (Figure S2).

In the spectroelectrochemical experiments, we aimed at identifying the charge storage mechanisms, including capacitive charging, surface redox, and intercalation first by cyclic voltammetry. The associated coloration mechanisms during charging, such as redox-based polaronic formation and nonredox LSPR absorption, were investigated by the absorbance spectra of the nanocrystals relative to different applied potentials in a progressive reduction. First, the nanocrystal films were cycled in both 0.5 M LiClO₄/PC and 0.5 M TBAClO₄/PC electrolytes for exploring their spectroelectrochemical properties and the influence of cation size. The reducing potentials used in different references were chosen to be approximately the same, relative to their respective reference potentials. The interpretation of cyclic voltammograms for the nanocrystal films in different conditions helps to understand the charge storage mechanisms first before moving on to the spectroelectrochemical properties. In the cyclic voltammograms scanned in 0.5 M LiClO₄/ PC (Figure 2a), the NPs show a rectangular wave with a weak signature of a redox peak, meaning the electrochemistry is dominated by capacitive charging.¹⁷ In this mechanism, upon electrochemical reduction, Li⁺ is desolvated and adsorbed on the surface of NPs to balance the additional charge.⁴⁰ The slight deviation from an ideal rectangular wave could be due to the reaction of impurities in the PC electrolyte solution such as a trace amount of water or 1,2-propanediol. ⁴¹ In Figure 2b, the cyclic voltammogram of NPs in 0.5 M TBAClO₄/PC is consistent with the case in Li+ and can be attributed to the same capacitive charging mechanism. On the other hand, in Figure 2a, the cyclic voltammogram waves of NRs and NPLs are flat at higher potential (between 4 and 2.2 V (vs Li/Li⁺)) due to capacitive charging, but show distinctive redox peaks

with larger absolute current density in the lower potential region (between 2.2 and 1.5 V (vs Li/Li+)), corresponding to the reduction of Nb5+ and the reoxidation of reduced Nb4+. The cyclic voltammograms of NRs and NPLs in 0.5 M TBAClO₄/PC (Figure 2b) are similar to the case in Li⁺ except that the two redox peaks in NPLs were merged into one in TBA⁺ (Figure 2b). Quantitively, the redox of NRs and NPLs in TBA+ shows a decreasing absolute current density from redox in Li⁺. The electrochemical reaction of niobium(V) oxide can be described as the reduction of Nb5+ in concert with Li+ intercalation.⁴³ In the lower potential region in Figure 2a, the reduction of NRs and NPLs can further be separated into two peaks, a transitional peak at intermediate potential and a stronger reduction peak at a lower potential, which is commonly seen in niobium(V) oxides and can be attributed to the continuous reduction of Nb5+ occupying different lattice sites at decreasing potential along with an increasing amount of intercalated Li $^{+}$. 44,45 On the other hand, considering the size of TBA+ (0.415 nm) and the size of basic structural motifs in niobium(V) oxides, the niobium octahedra (NbO6, ~0.4 nm), 46,47 the intercalation of TBA+ is difficult compared to Li+. We therefore attributed the redox peaks of NRs and NPLs in the lower potential region in Figure 2b to the reduction of Nb⁵⁺ balanced by TBA⁺ adsorbed on nanocrystal surfaces. The proposed surface redox mechanism in NRs and NPLs is analogous to that described in an earlier study using an electrochemical quartz crystal microbalance to analyze the redox mechanism of nanocrystalline anatase TiO₂ in both Li⁺ and TBA⁺, where a reversible mass change was observed in TBA+ compared to the irreversible mass increase in Li+ due to intercalation.²²

The absorbance spectra of NP, NR, and NPL films at different potentials were collected by reducing the nanocrystal films through chronoamperometry. This data set, coupled with the previously proposed charge storage mechanisms, was used to identify the coloration mechanism in different nanocrystals. In Figure 2c-e, the y-axis represents the difference in absorbance of the nanocrystal films reduced at different potentials from that in the transparent state at 4.0 V (vs Li/Li⁺) in 0.5 M LiClO₄/PC. In Figure 2c, a distinctive absorbance change peak in the near-infrared region rising along with decreasing potential can be observed in NPs, corresponding to their LSPR absorption.¹⁵ Notably, the absorbance change in Figure 2c increases continuously with decreasing potential and does not depend on redox reactions, a key feature associated with the capacitive charging in Figure 2a. The electrons accumulated during reduction contribute collectively to the LSPR absorption and the excess negative charge is balanced by the adsorbed Li⁺ in the EDL. On the contrary, in Figure 2d, the NRs increase their absorbance mostly in the near-infrared region after the onset of Nb⁵⁺ reduction at $\sim 1.8 \text{ V}$ (vs Li/Li⁺), corresponding to the redox peaks in Figure 2a that can be attributed to polaronic absorption.⁸ A similar progression was observed in Figure 2c for the spectra of NPLs during reduction. At potentials lower than 2.2 V (vs Li/Li⁺), we observed an increasing absorbance in the near-infrared region first, and at potentials lower than 1.7 V (vs Li/Li+), the absorbance increases mostly in the visible region. The dualmode electrochromism, which was previously reported, can be linked to the multiple redox events in NPLs seen in Figure 2a leading to free carrier and then polaronic absorption.¹⁰ Nevertheless, although the reduction of nanocrystal films in 0.5 M LiClO₄/PC elucidates whether the coloration

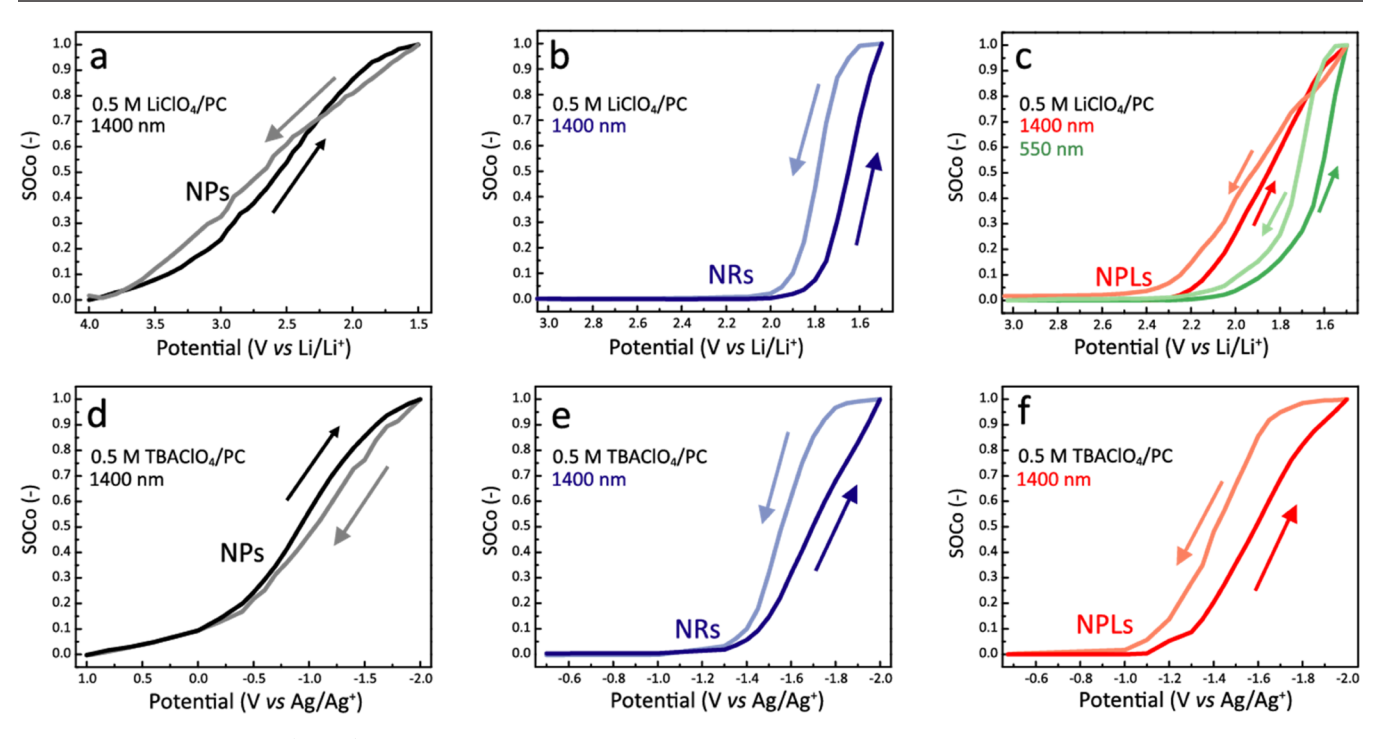


Figure 3. State of coloration (SOCo) at 1400 and 550 nm versus the potentials applied through chronoamperometry. The SOCo is defined as the ratio of absorbance change at a specific state to the maximum absorbance change at 1.5 V (vs Li/Li⁺) or -2.0 V (vs Ag/Ag⁺). (a, b, c) SOCo of the films of NPs, NRs, and NPLs reduced/oxidized at various potentials (vs Li/Li⁺) for 5 min in 0.5 M LiClO₄/PC. (d, e, f) SOCo of the films of NPs, NRs, and NPLs reduced/oxidized at various potentials (vs Ag/Ag⁺) for 5 min in 0.5 M TBAClO₄/PC.

mechanism was brought by redox reactions, the differentiation between surface redox and intercalation requires additional evidence.

The aim of comparing the absorbance change spectra in both Li⁺ and TBA⁺ is to differentiate the aforementioned three charge storage mechanisms. Figure 2f-h shows the differential absorbance spectra of nanocrystal films reduced at different potentials referenced to their respective absorbance spectra at 1.0 V (vs Ag/Ag⁺) in 0.5 M TBAClO₄/PC. In Figure 2f, the increasing absorbance change of NPs is consistent with the spectra shown in Figure 2c showing features of capacitive charging that are not sensitive to the size of cations. Similarly, for NRs (Figure 2g), the absorbance change in TBA⁺ increases along with the redox peaks shown in Figure 2b. This suggests that although the TBA⁺ is too large to intercalate into the NRs, the adsorption of desolvated TBA+ on the NR surface can still balance the additional negative charge from the reduction of Nb⁵⁺. The absorbance changes induced by this redox event occur at potentials lower than -1.4 V (vs Ag/Ag⁺) (Figure 2g). Additionally, the reduction in Li⁺ gives rise to a slightly larger absorbance change between 1400 and 1600 nm than the region between 1000 and 1200 nm (Figure 2b), whereas in TBA⁺ the tilt of the spectral lineshape is the opposite (Figure 2g). This implies that upon the reduction of Nb⁵⁺, the difference in charge storage mechanism can lead to changes in the spectral features for the polaronic absorption, as demonstrated here for the difference between surface redox in TBA⁺ and intercalation in Li⁺. For the NPLs, when reduced in TBA+ (Figure 2h), the absorbance change increases mostly in the near-infrared region and is dependent on reduction, occurring at potentials lower than -1.1 V (vs Ag/Ag⁺), again attributed purely to surface redox. When reduced in Li+ (Figure 2e), the absorbance initially rises in the near-infrared region first, aligning well with the spectral change seen in TBA⁺

(Figure 2h). Further reduction in Li⁺ only gives rise to the secondary absorption that increases absorbance mostly in the visible region. This visible absorption specifically occurs when Li⁺ intercalates in the NPLs, which is prohibited by the large size of TBA⁺. The spectral changes of NRs and NPLs when reduced in Li⁺ agree well with our previous publications and the electrochemical reduction of Nb⁵⁺ in both materials was verified by X-ray photoelectron spectroscopy. ^{8,10} For both NRs and NPLs, the absorbance change in TBA⁺ is smaller than under the same conditions in Li⁺, consistent with the smaller absolute current density in cyclic voltammograms.

The NPs exemplify the coloring mechanism activated by the capacitive charge storage mechanism, where charge accumulates and absorbance increases continuously as potential decreases, regardless of cation size. The coloration mechanism associated with this phenomenon can be attributed to LSPR absorption. As for the NRs and NPLs, the visible absorbance change comes from the redox of NbS+, where we observed increasing absorbance only at substantially low potential, leading to the absorption from polaron formation, while at more moderate reducing potential, free carrier absorption occurs in NPLs. Precisely, redox processes can be further separated into two charge storage mechanisms, surface redox and ion intercalation. By reducing the nanocrystal films in electrolytes containing cations of different sizes, we demonstrated in the case of NPLs that the additional electrochromic absorption in the visible region is only allowed in Li⁺ due to ion intercalation but not in TBA+ due to its bulky nature. Hence, the seemingly similar charge storage mechanisms in cyclic voltammograms can be distinguished by observing the electrochromic spectral change of the nanocrystal films.

The relationship between the applied potential and absorbance change at a specific wavelength was extracted to better visualize the difference between the coloration triggered

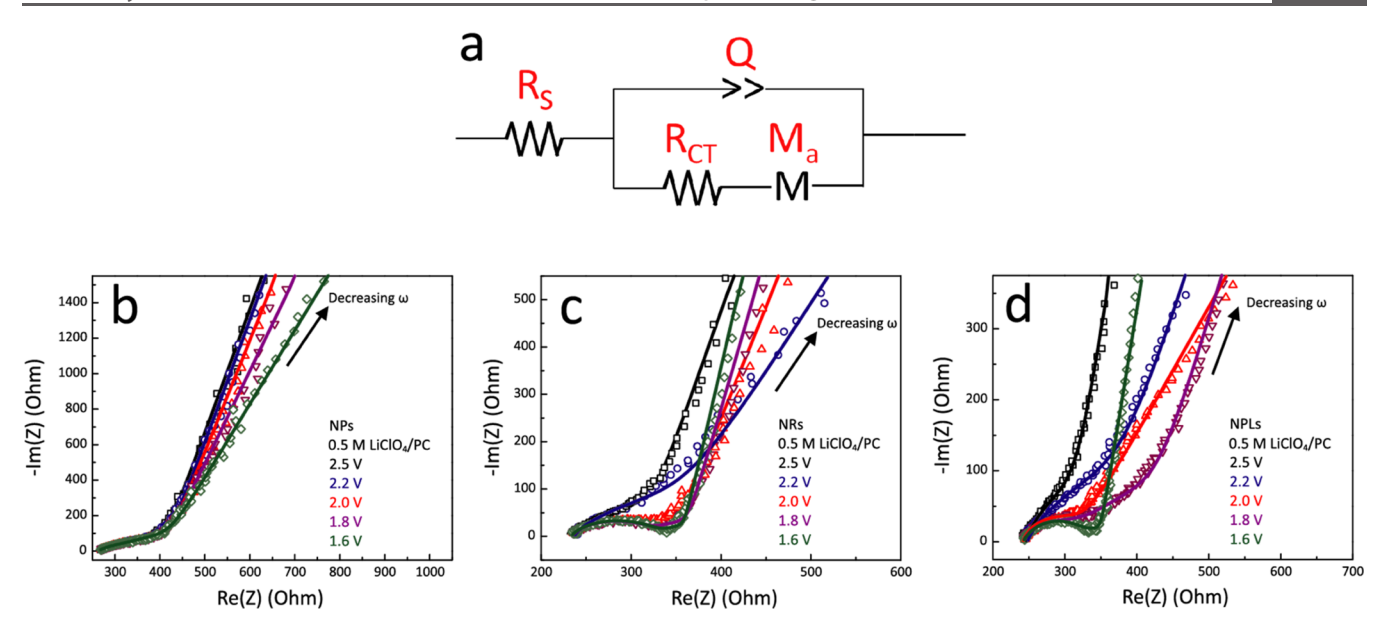


Figure 4. (a) Equivalent circuit used to model the electrochemical impedance spectroscopy (EIS) spectra. This circuit was modified from a Randles circuit, with R_s being the serial resistance, R_{ct} being the charge transfer resistance of redox reactions, M_a being the modified restricted diffusion element of Warburg diffusion, and Q being the constant phase element of the capacitive part in redox reactions. (b, c, d) Experimental EIS spectra (scatter) of the films of NPs, NRs, and NPLs at various potentials (vs Li/Li⁺) in 0.5 M LiClO₄/PC and the fitted spectra (lines) modeled using the equivalent circuit.

by capacitive charging or redox reaction. The magnitude of the absorbance change at different potentials, in both reduction and oxidation, is plotted in Figure 3 where the state of coloration (SOCo) is defined as the ratio of absorbance change at a specific state to the maximum absorbance change at 1.5 V (vs Li/Li⁺ in 0.5 M LiClO₄/PC) or -2.0 V (vs Ag/Ag⁺ in 0.5 M TBAClO₄/PC).⁵ In this experiment, the nanocrystal films were first gradually reduced from the transparent state to the most reduced potential and then oxidized back. Regardless of applied potentials, the SOCo of NPs increases/decreases steadily along with reducing/oxidizing potentials in both Li⁺ and TBA+ (Figure 3a,d). By contrast, the NRs and NPLs show increasing SOCo only at a substantially low potential (Figure 3b,c,e,f), suggesting that the coloration of NRs and NPLs is correlated strongly to the reduction of Nb5+. The SOCo change of NPLs films in Li⁺ can be further separated into the visible (550 nm) and the near-infrared (1400 nm) parts, corresponding to the dual-mode change in Figure 2e; the SOCo at 550 nm starts increasing at much lower potentials (Figure 3c). It is worth noting that in Figure 3, in one completed cycle of reduction and oxidation, we observed the SOCo hysteresis in both NRs and NPLs, which we believe is a signature of redox reactions. Even at the same potential, the SOCo during the forward scan differs from that at the reverse scan, consistent with the separation of reduction and oxidation peaks in cyclic voltammograms.

We collected electrochemical impedance spectroscopy (EIS) spectra of the nanocrystal films in 0.5 M LiClO₄/PC to analyze their redox behavior at various potentials (vs Li/Li⁺). The EIS spectra of the films of NPs, NRs, and NPLs and the equivalent circuit used to fit the EIS spectra are presented in Figure 4 and the fitting parameters are reported in Table S1. The EIS spectra were fit using a modified Randles circuit (Figure 4a), which is a commonly used model for metal oxide electrodes that includes a redox reaction and a Warburg diffusion element in series with the charge transfer resistance from the redox reaction. In Figure 4b, the NPs show almost identical EIS

spectra at different potentials. A small semicircle was observed at high frequency, and at low frequency, the impedance increases linearly with lowering frequency, a signature of Warburg diffusion. In comparison, in Figure 4c,d, the NRs and NPLs show similar behavior to NP films at higher applied potential (2.5 V (vs Li/Li⁺)), while at lower potentials, we observed the development of a semicircle, a feature of redox reaction (which is absent in NPs) due to the reduction of Nb⁵⁺. By monitoring the development of a semicircle in the EIS spectra, we demonstrate the transition of EIS spectra from capacitive charging to redox reaction in nanocrystal films. In brief conclusion, by comparing the results in Figures 3 and 4, the NP films show consistently capacitive charging behavior throughout the reduction and a continuous increase in SOCo (Figure 3a), whereas for NRs and NPLs, the initial reduction gives rise to a capacitive charging feature at 2.5 V (vs Li/Li⁺) that does not contribute to coloration, and at lower potentials, the emergence of a semicircle in EIS corresponds to the reduction of Nb5+, triggering increasing SOCo. These observations form the basis for analyzing the electrochromic switching kinetics of the three types of nanocrystals.

Electrochromic Switching Kinetics. Next, we sought to determine the electrochromic switching kinetics of nanocrystal films with different charge storage mechanisms. In Figures 2, 3, and 4, we established the charge storage mechanisms of NPs, NRs, and NPLs that trigger their electrochromic absorption. Nevertheless, the kinetics of the charging event can be more complicated. For example, during capacitive charging leading to the formation of an EDL, the desolvated ions can be both adsorbed on the surface or into the pores between the nanocrystals in the film,40 leading to the formation of a nanoconfined EDL. Likewise in redox reactions, we know the ions can be adsorbed on the surface or intercalating into the nanocrystals, representing two very different mechanisms with different implications for charging kinetics. Our goal is to systematically understand the impact of these mechanisms by modeling the electrochromic change over time with an

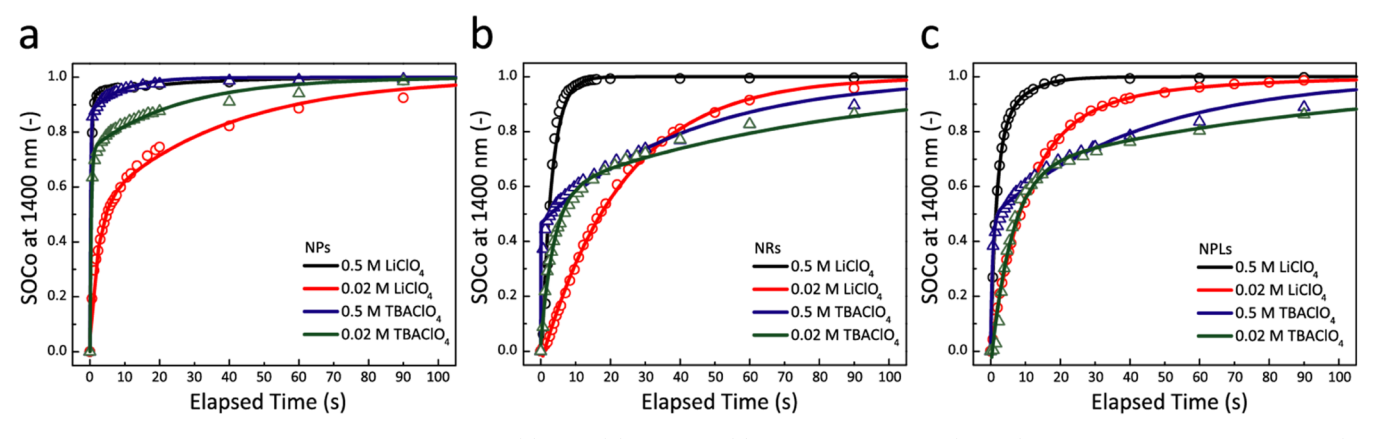


Figure 5. SOCo over time at 1400 nm for the films of (a) NPs, (b) NRs, and (c) NPLs. The raw data (scatter) were collected by applying 1.5 V (vs Li/Li⁺) to the nanocrystal films through chronoamperometry in different electrolyte concentrations, including 0.5 M LiClO₄ (black), 0.02 M LiClO₄ (red), 0.5 M TBAClO₄ (blue), and 0.02 M TBAClO₄ (green). Fitting results (solid lines) in different conditions were plotted alongside the raw data.

equation that can account for several mechanisms simultaneously. We started with the equation that correlates the charge capacity (Q) over time in capacitors charged at a constant potential⁴⁹

$$Q = E^* C_{\rm d}^* [1^- \exp(-t/\tau)] \tag{1}$$

where E is the applied potential, $C_{\rm d}$ is the EDL capacitance, t is the elapsed time, and τ is the time constant ($\tau=R*C_{\rm d}$, where R is the resistance). In an ideal situation neglecting leakage current, we assume that the charge injected into a nanocrystal film equals the increasing concentration of electrochromic chromophores ($\Delta Q = \Delta c$), and according to the Beer–Lambert law, the absorbance change is proportional to the increasing concentration of chromophores ($\Delta A \propto \Delta c$). We further simplified ΔA by introducing the state of coloration (SOCo) that equals the fractional absorbance change compared to the maximum absorbance change during reduction. The linear relationship between SOCo and ΔQ leads to eq 2.

$$SOCo = a^*[1 - \exp(-t/\tau)]$$
 (2)

where a is the pre-exponent factor proportional to E and $C_{\rm d}$. eq 2 describes how SOCo depends on the elapsed time after the initial application of a reducing potential. By using SOCo to analyze the dynamic spectral response, we focus specifically on the coloration of the nanocrystals, while the overall capacity change can also include contributions from leakage current. Considering that there could be a multistage mechanism that governs the switching kinetics of nanocrystal films, eq 2 can be further expanded to eq 3 for modeling kinetics with varying switching rates in different time scales

SOCo =
$$a_1^*[1 - \exp(-t/\tau_1)] + a_2^*[1 - \exp(-t/\tau_2)]$$
 (3)

Using this multiexponential-growth equation allows for the possibility of varying kinetics during electrochromic switching.

We use this equation to model the change of SOCo over time during the application of a constant reducing potential. Fitting based on eq 3 implies that the change of SOCo over time is controlled by a series of charging events sharing a similar mechanism to the charging of capacitors. Figure S3 shows an example of raw data fitted by eq 3. By separately plotting the two components in eq 3, we can observe the

contribution from a faster switching on a shorter time scale and a slower switching on a longer time scale. This methodology was applied to the switching kinetics of nanocrystal films, as discussed in the next paragraph.

The switching kinetics of nanocrystal films were measured by applying 1.5 V (vs Li/Li⁺) to reduce the films and the SOCo was recorded in situ over time (Figure 5). We tested the switching kinetics of films in both Li⁺- and TBA⁺-based electrolytes to determine the influence of ion intercalation. We also considered the effect of electrolyte concentration, in part because in eq 3, the time constant τ is known to be affected by the resistance R, a parameter describing the bulk electrolyte resistance that increases for decreasing electrolyte concentration. ⁵⁰ In Figure 5, the raw kinetic data (scatter data) were fitted by eq 3 (solid lines), and the fitting parameters were collected in Table S2.

The switching kinetics of NPs show a distinctive dual-stage signature (Figure 5a). The films reach a high SOCo in a short time scale (<10 s), but to achieve full coloration (SOCo ~ 0.95), a much longer time was required especially for the low electrolyte concentration. As for the influence of cation size, we observed the same dual-stage switching but faster switching kinetics when the NPs were reduced in TBA⁺. Quantifying this observation using fitting based on eq 3, in 0.5 M LiClO₄/PC, we see that the time constant in the first component of eq 3 (τ_1 = 0.36 s) is much smaller than the time constant in the second component (τ_2 = 24.3 s). This result also holds for NPs in other conditions regardless of cation size and electrolyte concentration (Table S2). The difference between the kinetics for varying electrolyte concentrations is ascribed to the resistance R that increases the time constant. By decreasing electrolyte concentration, the increasing solution resistance leads to a slower (larger) time constant, thus slower kinetics. The TBAClO₄/PC electrolyte having a slightly higher ionic conductivity compared to the LiClO₄/PC electrolyte could be the result of a faster response, according to literature, suggesting that the degree of electrolyte dissociation can be proportional to the reciprocal of ionic radii. 30,51,52 For the dual-stage switching, in the earlier discussion, we determined that the electrochemical mechanism of NPs is governed by capacitive charging. The increasing time constant implies that during reduction, the NPs require a longer time to accumulate the EDL and the associated absorbance change. Hence, in NPs, the switching kinetics are controlled by the formation of the

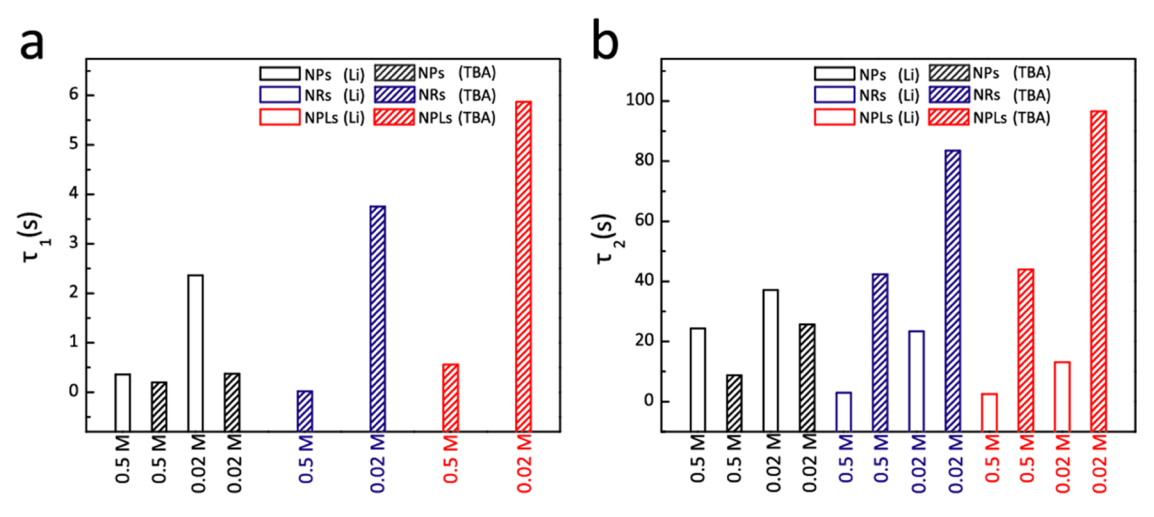


Figure 6. Fitting parameters, (a) τ_1 and (b) τ_2 , for the switching kinetics of the films of NPs, NRs, and NPLs based on eq 3. The fitting parameters of NPs (black), NRs (blue), and NPLs (red) were obtained by fitting the kinetic data in both LiClO₄/PC (open bars) and TBAClO₄/PC (filled bars).

EDL and we propose that the dual-stage switching mechanism (Figure 5a) arises because of the increased thickness of EDL during capacitive charging.⁵³ At reducing potentials, both SOCo and surface charge density increase due to the injection of electrons.⁵³ This process leads to the increase of EDL thickness over time and results in a secondary, slower process since the addition of new cations diffusing through the EDL would be slower compared to the initial stage. Similar phenomena were observed during capacitive charging in other electrochemical systems such as charging of porous electrodes and the formation of EDL by bulky ionic liquids. 54-56 Typically in porous electrodes with large capacitance, the charging dynamics can exhibit two relaxation time scales governed by a traditional capacitor charging and a diffusion-controlled process, corresponding to the SOCo change in shorter and longer time scales, respectively.

For NRs and NPLs, redox reactions govern the electrochromic switching kinetics and we observe distinctive dual-stage switching kinetics when reducing the films in TBA⁺, while in Li⁺, a single component accounts for the kinetics (Figure 5b,c). For the latter case, when fitting to eq 3, the fitting parameters τ_1 and τ_2 are the same. When reducing the NRs in 0.5 M TBAClO₄/PC, a faster switching with τ_1 = 0.02 s and a slower switching with τ_2 = 42.4 s were obtained. Upon reducing the NRs in 0.5 M LiClO₄/PC, only one switching with τ = 2.9 s results from fitting. Other parameters for the fittings in Figure 5b,c were also collected in Table S2. The sole kinetic constants from the reduction of NRs and NPLs films in Li⁺ correspond to the slower component of the dual-stage mechanism, limited by the ion diffusion rate.

The switching kinetics of NRs and NPLs films in TBA⁺ exhibit dual-stage switching, similar to that seen for NPs, implying that the aforementioned mechanism based on EDL formation may still apply. Consistent with this hypothesis, decreasing electrolyte concentration leads to the increasing time constant, as before. The most notable difference between the switching of NRs and NPLs in TBA⁺ compared to the switching of NPs is that the magnitude of τ_2 in NRs and NPLs is much larger than the τ_2 in NPs. Because the coloring mechanism of NRs and NPLs is related to surface redox reactions, their absorbance changes require larger charge capacity, as evidenced by the larger cathodic current density in

Figure 2b. The larger τ_2 suggests that adding additional TBA⁺ for charge balance at relatively high SOCo is more sluggish in a surface redox mechanism compared to capacitive charging, potentially due to the difficulty to have TBA⁺ traveling through a thicker EDL.

Conversely, the switching kinetics of NRs and NPLs in Li⁺ show single-stage switching kinetics that can be fitted by only one exponential-growth component in eq 3. We observe faster switching in 0.5 M LiClO₄/PC (τ_2 = 2.89 for NRs and 2.58 for NPLs) but much slower switching in 0.02 M LiClO₄/PC (τ_2 = 23.5 for NRs and 13.1 for NPLs) due to the decreasing electrolyte concentration (Figure 5b,c). According to our earlier analysis, the electrochromic response of NRs and NPLs in Li⁺ is triggered by redox reactions and the Li⁺ can be desolvated and intercalated into the crystal lattice of the NRs and NPLs. 43 In this case, the additional charge from the reduction of Nb5+ will be mostly balanced by the intercalated Li⁺. The involvement of Li⁺ intercalation changes the mechanism drastically and only one switching rate is observed. The microscopic processes that govern the kinetics can be the diffusion of Li⁺, as traditionally suggested for bulk materials, or other factors that could change the reaction rate of Nb5+ reduction such as electron transport within the nanocrystal films. Based on the significantly increased τ_2 at decreasing electrolyte concentration, the limiting factor of the switching mechanism can be attributed to the kinetics of electrochemical redox at the nanocrystal/electrolyte interface.⁵

The kinetic data for the oxidation/bleaching process were collected by applying 4.0 V (vs Li/Li⁺) to the nanocrystal films after the reducing step and monitoring the SOCo. The oxidation switching kinetics are in general much faster than the reduction process (Figure S4). The nanocrystal films can reach a significantly low SOCo within 10 s except for the NPLs that show slightly slower switching kinetics. This asymmetry implies that, in a reversed situation where the ions are pulled out from the working electrode, identifying the rate-limiting factors, such as the removal of EDL or the ion deintercalation, is relatively difficult compared to the coloring process because the variables (cation size and concentration) do not play an important role in limiting the switching kinetics.

For NPLs, monitoring the SOCo at 550 nm instead of 1400 nm when charging and discharging in Li⁺ reveals kinetics

associated with Li⁺ intercalation that is not allowed in TBA⁺. The switching at 550 nm is roughly 3 times slower in τ_2 when compared to the switching at 1400 nm, indicating slower kinetics at higher intercalation levels resulting in the absorption in the visible region (Figure S5), compared to the lower-level Li⁺ intercalation giving rise to near-infrared absorption.

The values of fitting parameters τ_1 and τ_2 were plotted in Figure 6a,b to better compare the interplay of charge storage mechanism, cation size, and electrolyte concentration in the nanocrystal films. τ_1 represents the efficient switching kinetics of nanocrystal films in a shorter time period (<10 s). This process corresponds to the early stage of EDL formation in the electrochromic response of NPs supported by capacitive charging and the electrochromic response of NRs and NPLs supported by surface redox only in TBA⁺. The value of τ_1 is associated with the ionic conductivity of the electrolyte that can be controlled by electrolyte concentration and more subtly by cation size. When comparing the τ_1 between capacitive charging and surface redox, we noticed that the decreasing electrolyte concentration significantly drags down the switching kinetics in surface redox, while it shows only moderate influence in capacitive charging, potentially due to a larger capacity required to increase the SOCo in surface redox. The slower kinetic time constant τ_2 roughly doubles regardless of materials when decreasing the electrolyte concentration. The nature of the slower kinetic processes in the surfacerelated mechanisms including surface redox and capacitive charging could be attributed to the increasing thickness of EDL on a longer time scale. On the contrary, for the τ_2 of NRs and NPLs when reduced in Li⁺ (Figure 6b), single switching kinetics were obtained, corresponding to the reaction rate of Li⁺ intercalation. In addition, the influence of Li⁺ intercalation was investigated by comparing the SOCo of the NPLs at 550 nm, where intercalation dominates, to the SOCo at 1400 nm. Switching at 550 nm has 3 times larger τ_2 compared to τ_2 at 1400 nm (Figure S5 and Table S2). The pre-exponential factors a_1 and a_2 (Figure S6) determine the relative weight of the corresponding switching kinetics in the coloration reaction. For example, the switching of NP films in 0.5 M LiClO₄/PC and 0.5 M TBAClO₄/PC is highly efficient and can reach almost 0.95 SOCo within the first few seconds of reduction (Figure 5a). Therefore in Figure S6, the said switching kinetics show a higher a_1 (~0.9) compared to a_2 (~0.1). On the contrary, the reduction of NPs in 0.02 M LiClO₄/PC shows comparable a_1 (0.46) and a_2 (0.49), indicating that the slower kinetics with a much higher time constant become more prominent during switching. In redox-governed kinetics for NRs and NPLs, when reduced in TBA⁺, the said trend is not as obvious as in NPs. We observed slightly lower a_1 and slightly higher a_2 in the electrolyte with higher concentrations.

The three charge storage mechanisms we observed during the electrochromic switching of the films of NPs, NRs, and NPLs are summarized schematically in Figure 7. In the capacitive charging process during the switching of NPs, the cations were desolvated and adsorbed on the nanocrystal surface to balance the negatively charged surface. The charging process is governed by the formation of an EDL, where the inner layer consists of desolvated cations, subsequently balanced by an outer layer consisting of solvated ions attracted by electrostatic interactions. The optical switching kinetics of NPs thus show dual-stage switching kinetics due to capacitive charging, where the development of the EDL slows down the kinetics over time. It is worth noting that the formation of an

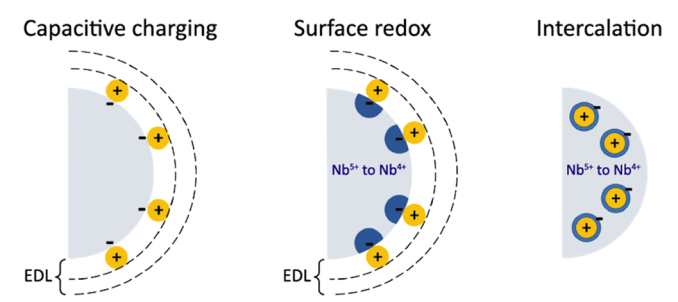


Figure 7. Schematic representation of capacitive charging, surface redox, and intercalation charge storage mechanisms that drive the electrochromic response of nanocrystal films.

EDL also occurs in the NRs and NPLs, but as evidenced in Figure 2, capacitive charging contributes to minimum absorbance change in NRs and NPLs. Instead, the electrochromic responses of NRs and NPLs films are dominated by redox reactions, either surface redox in TBA+ or intercalation in Li⁺. In the surface redox mechanism, we proposed that the structure found near the nanocrystal surface would be similar to the EDL structure, meaning the charge brought by the reduction of Nb⁵⁺ will be balanced by the inner layer EDL as well, leading to dual-stage switching kinetics. Although, the electronic charge can be localized at transition-metal ions near the surface, unlike the delocalized charging that occurs in NPs when they are capacitively charged. On the contrary, the intercalation process involves the insertion of desolvated Li⁺ into the nanocrystals to compensate for the charge added to reduce Nb5+, leading to single-stage switching kinetics.

By collecting the kinetic data of SOCo over time and fitting the data in various conditions by eq 3, we concluded several observations that can be helpful for improving the design of nanoscale electrochromic materials with a shorter switching time. The switching kinetics of capacitive charging depend solely on the ionic conductivity of the electrolyte, and to minimize the time constant, a higher electrolyte concentration is preferred. On the other hand, for switching kinetics governed by redox reactions, it is important to understand whether intercalation is allowed. If the switching kinetics are driven only by surface redox, a prolonged switching time will likely be observed due to the increasing EDL thickness following increasing nanocrystal surface charge density. Instead, switching controlled by ion intercalation is often faster at sufficiently high electrolyte concentration.

CONCLUSIONS

In this research, we systematically investigated the dynamic electrochromic response activated by different charge storage mechanisms in the films of three metal oxide nanocrystals, including NPs, NRs, and NPLs. By studying the cyclic voltammograms of the nanocrystals, we identified the signature of redox reactions in NRs and NPLs compared to the pure capacitive charging behavior in NPs. Alongside the electrochemical analysis, the change of the absorbance spectrum of the nanocrystals during reduction in both Li⁺ and TBA⁺ was collected to reveal the electrochromic signature of capacitive charging and redox reactions. The use of cations with different sizes enables us to distinguish between surface redox and ion intercalation, both showing similar electrochemical signatures but the absorption mode from ion intercalation is only allowed in Li⁺ but not in TBA⁺. The switching kinetics of capacitive charging (in NPs), surface redox (in NRs and NPLs when

reducing in TBA⁺), and intercalation (in NRs and NPLs when reducing in Li⁺) were quantified by fitting the SOCo over time with an exponential-growth equation, allowing us to compare the efficiency of each mechanism in various conditions by its time constant. The measurement of switching kinetics suggests that in surface-dominated capacitive charging and surface redox, regardless of the materials and cations, the ionic conductivity determines the time constants. Notably, we also observed a dual-stage switching mechanism with faster kinetics on a short time scale but characteristically slower kinetics on a longer time scale, corresponding to the accumulation of the EDL. On the contrary, single-stage switching kinetics were observed in the electrochromic response governed by Li⁺ intercalation. Overall, our results provide a methodology to define the charge storage mechanisms in metal oxide nanocrystals and study the mechanisms of associated electrochromic switching kinetics that can be applied to the design of electrochromic smart windows for minimizing switching time.

ASSOCIATED CONTENT

Supporting Information

The Supporting Information is available free of charge at https://pubs.acs.org/doi/10.1021/acs.chemmater.2c00930.

Atomistic models used for calculated XRD patterns, SEM images of the nanocrystal films, sample data for demonstrating the fitting of the switching kinetic data, the plots of SOCo over time in the oxidizing/bleaching process of the nanocrystal films, the SOCo over time at 550 nm for NPL films, the pre-exponent factors from the fitting of the switching kinetic data, and the tables for the fitted parameters in EIS spectrum fitting and switching kinetic data fitting are shown in Supporting Information (PDF)

AUTHOR INFORMATION

Corresponding Author

Delia J. Milliron – McKetta Department of Chemical Engineering, The University of Texas at Austin, Austin, Texas 78712-1589, United States; Department of Chemistry, The University of Texas at Austin, Austin, Texas 78712-1589, United States; orcid.org/0000-0002-8737-451X; Email: milliron@che.utexas.edu

Authors

Hsin-Che Lu − McKetta Department of Chemical Engineering, The University of Texas at Austin, Austin, Texas 78712-1589, United States; orcid.org/0000-0001-5673-2647

Benjamin Z. Zydlewski — Department of Chemistry, The University of Texas at Austin, Austin, Texas 78712-1589, United States; © orcid.org/0000-0001-5591-1731

Bharat Tandon — McKetta Department of Chemical Engineering, The University of Texas at Austin, Austin, Texas 78712-1589, United States; orcid.org/0000-0003-1108-9859

Sofia A. Shubert-Zuleta – Department of Chemistry, The University of Texas at Austin, Austin, Texas 78712-1589, United States; orcid.org/0000-0003-0445-175X

Complete contact information is available at: https://pubs.acs.org/10.1021/acs.chemmater.2c00930

Notes

The authors declare the following competing financial interest(s): D.J.M. has a financial interest in Heliotrope Technologies, a company pursuing the commercial development of electrochromic devices.

ACKNOWLEDGMENTS

The authors acknowledge support from Companhia Brasileira de Metalurgia e Mineração (CBMM), the National Science Foundation (CHE-1905263), and the Welch Foundation (F-1848).

REFERENCES

- (1) Wang, Y.; Runnerstrom, E. L.; Milliron, D. J. Switchable Materials for Smart Windows. *Annu. Rev. Chem. Biomol. Eng.* **2016**, 7, 283–304.
- (2) Runnerstrom, E. L.; Llordés, A.; Lounis, S. D.; Milliron, D. J. Nanostructured Electrochromic Smart Windows: Traditional Materials and Nir-Selective Plasmonic Nanocrystals. *Chem. Commun.* **2014**, *50*, 10555–10572.
- (3) Niklasson, G. A.; Granqvist, C. G. Electrochromics for Smart Windows: Thin Films of Tungsten Oxide and Nickel Oxide, and Devices Based on These. *J. Mater. Chem.* **2007**, *17*, 127–156.
- (4) Wang, J.; Polleux, J.; Lim, J.; Dunn, B. Pseudocapacitive Contributions to Electrochemical Energy Storage in Tio₂ (Anatase) Nanoparticles. *J. Phys. Chem. C* **2007**, *111*, 14925–14931.
- (5) Dahlman, C. J.; Heo, S.; Zhang, Y.; Reimnitz, L. C.; He, D.; Tang, M.; Milliron, D. J. Dynamics of Lithium Insertion in Electrochromic Titanium Dioxide Nanocrystal Ensembles. *J. Am. Chem. Soc.* **2021**, *143*, 8278–8294.
- (6) Kim, K.-W.; Yun, T. Y.; You, S.-H.; Tang, X.; Lee, J.; Seo, Y.; Kim, Y.-T.; Kim, S. H.; Moon, H. C.; Kim, J. K. Extremely Fast Electrochromic Supercapacitors Based on Mesoporous Wo₃ Prepared by an Evaporation-Induced Self-Assembly. *NPG Asia Mater.* **2020**, *12*, No. 84.
- (7) Heo, S.; Kim, J.; Ong, G. K.; Milliron, D. J. Template-Free Mesoporous Electrochromic Films on Flexible Substrates from Tungsten Oxide Nanorods. *Nano Lett.* **2017**, *17*, 5756–5761.
- (8) Ong, G. K.; Saez Cabezas, C. A.; Dominguez, M. N.; Skjærvø, S. L.; Heo, S.; Milliron, D. J. Electrochromic Niobium Oxide Nanorods. *Chem. Mater.* **2020**, 32, 468–475.
- (9) Lu, H.-C.; Katyal, N.; Henkelman, G.; Milliron, D. J. Controlling the Shape Anisotropy of Monoclinic $Nb_{12}o_{29}$ Nanocrystals Enables Tunable Electrochromic Spectral Range. *J. Am. Chem. Soc.* **2021**, *143*, 15745–15755.
- (10) Lu, H.-C.; Ghosh, S.; Katyal, N.; Lakhanpal, V. S.; Gearba-Dolocan, I. R.; Henkelman, G.; Milliron, D. J. Synthesis and Dual-Mode Electrochromism of Anisotropic Monoclinic Nb₁₂o₂₉ Colloidal Nanoplatelets. *ACS Nano* **2020**, *14*, 10068–10082.
- (11) Cai, G.; Zhu, R.; Liu, S.; Wang, J.; Wei, C.; Griffith, K. J.; Jia, Y.; Lee, P. S. Tunable Intracrystal Cavity in Tungsten Bronze-Like Bimetallic Oxides for Electrochromic Energy Storage. *Adv. Eng. Mater.* **2022**, *12*, No. 2103106.
- (12) Evans, R. C.; Ellingworth, A.; Cashen, C. J.; Weinberger, C. R.; Sambur, J. B. Influence of Single-Nanoparticle Electrochromic Dynamics on the Durability and Speed of Smart Windows. *Proc. Natl. Acad. Sci. U.S.A.* **2019**, *116*, 12666–12671.
- (13) Dahlman, C. J.; Tan, Y.; Marcus, M. A.; Milliron, D. J. Spectroelectrochemical Signatures of Capacitive Charging and Ion Insertion in Doped Anatase Titania Nanocrystals. *J. Am. Chem. Soc.* **2015**, *137*, 9160–9166.
- (14) Luo, Z.; Liu, L.; Yang, X.; Luo, X.; Bi, P.; Fu, Z.; Pang, A.; Li, W.; Yi, Y. Revealing the Charge Storage Mechanism of Nickel Oxide Electrochromic Supercapacitors. *ACS Appl. Mater. Interfaces* **2020**, *12*, 39098–39107.
- (15) Garcia, G.; Buonsanti, R.; Runnerstrom, E. L.; Mendelsberg, R. J.; Llordes, A.; Anders, A.; Richardson, T. J.; Milliron, D. J.

- Dynamically Modulating the Surface Plasmon Resonance of Doped Semiconductor Nanocrystals. *Nano Lett.* **2011**, *11*, 4415–4420.
- (16) Heo, S.; Cho, S. H.; Dahlman, C. J.; Agrawal, A.; Milliron, D. J. Influence of Crystalline and Shape Anisotropy on Electrochromic Modulation in Doped Semiconductor Nanocrystals. *ACS Energy Lett.* **2020**, *5*, 2662–2670.
- (17) Gogotsi, Y.; Penner, R. M. Energy Storage in Nanomaterials Capacitive, Pseudocapacitive, or Battery-Like? *ACS Nano* **2018**, *12*, 2081—2083.
- (18) Wen, R.-T.; Malmgren, S.; Granqvist, C. G.; Niklasson, G. A. Degradation Dynamics for Electrochromic Wo₃ Films under Extended Charge Insertion and Extraction: Unveiling Physicochemical Mechanisms. ACS Appl. Mater. Interfaces 2017, 9, 12872–12877.
- (19) Ozkan, E.; Lee, S.-H.; Tracy, C. E.; Pitts, J. R.; Deb, S. K. Comparison of Electrochromic Amorphous and Crystalline Tungsten Oxide Films. *Sol. Energy Mater. Sol. Cells* **2003**, *79*, 439–448.
- (20) Özer, N.; Chen, D.-G.; Lampert, C. M. Preparation and Properties of Spin-Coated Nb₂o₅ Films by the Sol-Gel Process for Electrochromic Applications. *Thin Solid Films* **1996**, 277, 162–168.
- (21) Triana, C. A.; Granqvist, C. G.; Niklasson, G. A. Optical Absorption and Small-Polaron Hopping in Oxygen Deficient and Lithium-Ion-Intercalated Amorphous Titanium Oxide Films. *J. Appl. Phys.* **2016**, *119*, No. 015701.
- (22) Lyon, L. A.; Hupp, J. T. Energetics of Semiconductor Electrode/Solution Interfaces: Eqcm Evidence for Charge-Compensating Cation Adsorption and Intercalation During Accumulation Layer Formation in the Titanium Dioxide/Acetonitrile System. *J. Phys. Chem. A* **1995**, *99*, 15718–15720.
- (23) Wen, R.-T.; Granqvist, C. G.; Niklasson, G. A. Anodic Electrochromism for Energy-Efficient Windows: Cation/Anion-Based Surface Processes and Effects of Crystal Facets in Nickel Oxide Thin Films. *Adv. Funct. Mater.* **2015**, *25*, 3359–3370.
- (24) Long, J. W.; Qadir, L. R.; Stroud, R. M.; Rolison, D. R. Spectroelectrochemical Investigations of Cation-Insertion Reactions at Sol—Gel-Derived Nanostructured, Mesoporous Thin Films of Manganese Oxide. *J. Phys. Chem. B* **2001**, *105*, 8712–8717.
- (25) Zandi, O.; Agrawal, A.; Shearer, A. B.; Reimnitz, L. C.; Dahlman, C. J.; Staller, C. M.; Milliron, D. J. Impacts of Surface Depletion on the Plasmonic Properties of Doped Semiconductor Nanocrystals. *Nat. Mater.* **2018**, *17*, 710–717.
- (26) Heo, S.; Dahlman, C. J.; Staller, C. M.; Jiang, T.; Dolocan, A.; Korgel, B. A.; Milliron, D. J. Enhanced Coloration Efficiency of Electrochromic Tungsten Oxide Nanorods by Site Selective Occupation of Sodium Ions. *Nano Lett.* **2020**, *20*, 2072–2079.
- (27) Vijayalakshmi, R.; Jayachandran, M.; Trivedi, D. C.; Sanjeeviraja, C. Study of the Potassium Ion Insertion of the Electrodeposited Electrochromic Tungsten Trioxide Thin Films. *Ionics* **2004**, *10*, 151–154.
- (28) Zhang, S.; Cao, S.; Zhang, T.; Fisher, A.; Lee, J. Y. Al³⁺ Intercalation/De-Intercalation-Enabled Dual-Band Electrochromic Smart Windows with a High Optical Modulation, Quick Response and Long Cycle Life. *Energy Environ. Sci.* **2018**, *11*, 2884–2892.
- (29) Yaghoobnejad Asl, H.; Manthiram, A. Mass Transfer of Divalent Ions in an Oxide Host: Comparison of Mg²⁺ and Zn²⁺ Diffusion in Hexagonal K_xw₃o₉ Bronze. *Chem. Mater.* **2019**, *31*, 2296–2307.
- (30) Koh, A. R.; Hwang, B.; Chul Roh, K.; Kim, K. The Effect of the Ionic Size of Small Quaternary Ammonium Bf₄ Salts on Electrochemical Double Layer Capacitors. *Phys. Chem. Chem. Phys.* **2014**, *16*, 15146–15151.
- (31) Hu, H.; Hechavarría, L.; Campos, J. Optical and Electrical Responses of Polymeric Electrochromic Devices: Effect of Polyacid Incorporation in Polyaniline Film. *Solid State Ionics* **2003**, *161*, 165–172
- (32) Hassab, S.; Shen, D. E.; Österholm, A. M.; Da Rocha, M.; Song, G.; Alesanco, Y.; Viñuales, A.; Rougier, A.; Reynolds, J. R.; Padilla, J. A New Standard Method to Calculate Electrochromic Switching Time. Sol. Energy Mater. Sol. Cells 2018, 185, 54–60.

- (33) Tandon, B.; Shubert-Zuleta, S. A.; Milliron, D. J. Investigating the Role of Surface Depletion in Governing Electron-Transfer Events in Colloidal Plasmonic Nanocrystals. *Chem. Mater.* **2022**, *34*, 777–788.
- (34) Jansons, A. W.; Hutchison, J. E. Continuous Growth of Metal Oxide Nanocrystals: Enhanced Control of Nanocrystal Size and Radial Dopant Distribution. *ACS Nano* **2016**, *10*, 6942–6951.
- (35) Brown, P. J. F.; A G; Maslen, E. N.; O'Keefe, M. A.; Willis, B. T. M. Intensity of Diffracted Intensities. In *International Tables for Crystallography*, 1st ed.; Prince, E., Ed.; 2006; Vol. C, pp 554–595 DOI: 10.1107/97809553602060000600.
- (36) Murray, C. B.; Kagan, C. R.; Bawendi, M. G. Synthesis and Characterization of Monodisperse Nanocrystals and Close-Packed Nanocrystal Assemblies. *Annu. Rev. Mater. Sci.* **2000**, *30*, 545–610.
- (37) Momma, K.; Izumi, F. Vesta: A Three-Dimensional Visualization System for Electronic and Structural Analysis. *J. Appl. Crystallogr.* **2008**, *41*, 653–658.
- (38) Jhong, H.-R. M.; Nwabara, U. O.; Shubert-Zuleta, S.; Grundish, N. S.; Tandon, B.; Reimnitz, L. C.; Staller, C. M.; Ong, G. K.; Saez Cabezas, C. A.; Goodenough, J. B.; Kenis, P. J. A.; Milliron, D. J. Efficient Aqueous Electroreduction of Co₂ to Formate at Low Overpotential on Indium Tin Oxide Nanocrystals. *Chem. Mater.* **2021**, 33, 7675–7685.
- (39) Dong, A.; Ye, X.; Chen, J.; Kang, Y.; Gordon, T.; Kikkawa, J. M.; Murray, C. B. A Generalized Ligand-Exchange Strategy Enabling Sequential Surface Functionalization of Colloidal Nanocrystals. *J. Am. Chem. Soc.* **2011**, *133*, 998–1006.
- (40) Chmiola, J.; Largeot, C.; Taberna, P.-L.; Simon, P.; Gogotsi, Y. Desolvation of Ions in Subnanometer Pores and Its Effect on Capacitance and Double-Layer Theory. *Angew. Chem., Int. Ed.* **2008**, 47, 3392–3395.
- (41) Qian, Q.; Yang, Y.; Shao, H. Solid Electrolyte Interphase Formation by Propylene Carbonate Reduction for Lithium Anode. *Phys. Chem. Chem. Phys.* **2017**, *19*, 28772–28780.
- (42) Kodama, R.; Terada, Y.; Nakai, I.; Komaba, S.; Kumagai, N. Electrochemical and in Situ Xafs-Xrd Investigation of Nb₂o₅ for Rechargeable Lithium Batteries. *J. Electrochem. Soc.* **2006**, *153*, A583.
- (43) Augustyn, V.; Come, J.; Lowe, M. A.; Kim, J. W.; Taberna, P.-L.; Tolbert, S. H.; Abruña, H. D.; Simon, P.; Dunn, B. High-Rate Electrochemical Energy Storage through Li⁺ Intercalation Pseudocapacitance. *Nat. Mater.* **2013**, *12*, 518.
- (44) Chen, D.; Wang, J.-H.; Chou, T.-F.; Zhao, B.; El-Sayed, M. A.; Liu, M. Unraveling the Nature of Anomalously Fast Energy Storage in T-Nb₂o₅. *J. Am. Chem. Soc.* **2017**, *139*, 7071–7081.
- (45) Griffith, K. J.; Forse, A. C.; Griffin, J. M.; Grey, C. P. High-Rate Intercalation without Nanostructuring in Metastable Nb₂o₅ Bronze Phases. *J. Am. Chem. Soc.* **2016**, *138*, 8888–8899.
- (46) Ue, M. Mobility and Ionic Association of Lithium and Quaternary Ammonium Salts in Propylene Carbonate and Γ-Butyrolactone. *J. Electrochem. Soc.* **1994**, *141*, 3336–3342.
- (47) Jana, S.; Rioux, R. M. Seeded Growth Induced Amorphous to Crystalline Transformation of Niobium Oxide Nanostructures. *Nanoscale* **2012**, *4*, 1782–1788.
- (48) Bredar, A. R. C.; Chown, A. L.; Burton, A. R.; Farnum, B. H. Electrochemical Impedance Spectroscopy of Metal Oxide Electrodes for Energy Applications. *ACS Appl. Energy Mater.* **2020**, *3*, 66–98.
- (49) Bard, A. J.; Faulkner, L. R. Electrochemical Methods: Fundamentals and Applications; John Wiley & Sons: New York, 1980. (50) Zheng, J. P.; Jow, T. R. The Effect of Salt Concentration in Electrolytes on the Maximum Energy Storage for Double Layer Capacitors. J. Electrochem. Soc. 1997, 144, 2417–2420.
- (51) Laoire, C. O.; Mukerjee, S.; Abraham, K. M.; Plichta, E. J.; Hendrickson, M. A. Influence of Nonaqueous Solvents on the Electrochemistry of Oxygen in the Rechargeable Lithium—Air Battery. *J. Phys. Chem. C* **2010**, *114*, 9178–9186.
- (52) Seki, S.; Hayamizu, K.; Tsuzuki, S.; Takahashi, K.; Ishino, Y.; Kato, M.; Nozaki, E.; Watanabe, H.; Umebayashi, Y. Density, Viscosity, Ionic Conductivity, and Self-Diffusion Coefficient of

Chemistry of Materials Article pubs.acs.org/cm

Organic Liquid Electrolytes: Part I. Propylene Carbonate + Li, Na, Mg and Ca Cation Salts. J. Electrochem. Soc. 2018, 165, A542-A546. (53) Bohinc, K.; Kralj-Iglič, V.; Iglič, A. Thickness of Electrical Double Layer. Effect of Ion Size. Electrochim. Acta 2001, 46, 3033-

- (54) Lian, C.; Janssen, M.; Liu, H.; van Roij, R. Blessing and Curse: How a Supercapacitor's Large Capacitance Causes Its Slow Charging. Phys. Rev. Lett. 2020, 124, No. 076001.
- (55) Noh, C.; Jung, Y. Understanding the Charging Dynamics of an Ionic Liquid Electric Double Layer Capacitor Via Molecular Dynamics Simulations. Phys. Chem. Chem. Phys. 2019, 21, 6790-6800.
- (56) Kim, S. Y.; Jang, Y. J.; Kim, Y. M.; Lee, J. K.; Moon, H. C. Tailoring Diffusion Dynamics in Energy Storage Ionic Conductors for High-Performance, Multi-Function, Single-Layer Electrochromic Supercapacitors. Adv. Funct. Mater. 2022, n/a, No. 2200757.
- (57) Tian, R.; Park, S.-H.; King, P. J.; Cunningham, G.; Coelho, J.; Nicolosi, V.; Coleman, J. N. Quantifying the Factors Limiting Rate performance in Battery Electrodes. Nat. Commun. 2019, 10, No. 1933.

□ Recommended by ACS

How to Quantify Electrons in Plasmonic Colloidal Metal **Oxide Nanocrystals**

Sofia A. Shubert-Zuleta, Delia J. Milliron, et al.

MAY 02 2023

CHEMISTRY OF MATERIALS

READ 2

Ultranarrow Mid-infrared Quantum Plasmon Resonance of Self-Doped Silver Selenide Nanocrystal

Haemin Song, Kwang Seob Jeong, et al.

AUGUST 14, 2023

ACS NANO

READ

Subnanometer-Wide Indium Selenide Nanoribbons

William J. Cull, Andrei N. Khlobystov, et al.

MARCH 14, 2023

ACS NANO

READ **C**

Precursor-Mediated Colloidal Synthesis of Compositionally Tunable Cu-Sb-M-S (M = Zn, Co, and Ni) Nanocrystals and **Their Transport Properties**

Maria Zubair, Kevin M. Ryan, et al.

NOVEMBER 21, 2022

CHEMISTRY OF MATERIALS

READ **'**

Get More Suggestions >